Laterally varying scattering properties in the North Anatolian Fault Zone from ambient noise cross-correlations

Chantal van Dinther, Ludovic Margerin, Michel Campillo

1
2
3

Laterally varying scattering properties from ambient noise cross-correlations in the North Anatolian Fault Zone

5   **Chantal van Dinther[1], Ludovic Margerin[2]& Michel Campillo[1]**

6   [1]Université Grenoble Alpes, ISTerre, Grenoble, France

7   [2]Institut de Recherche en Astrophysique et Planétologie, Université Paul Sabatier, Toulouse, France

Corresponding author: Chantal van Dinther, `c.vandinther@gmail.com`

Abstract

Intrinsic absorption and scattering properties provide us with information about the physical state and heterogeneity of the Earth's crust. These properties are usually obtained by observing the energy decay of naturally occurring earthquakes, leading to sparse spatial sampling and therefore average scattering values over a large region. The present study uses ambient noise cross-correlations to analyse the energy decay and scattering properties over a part of the North Anatolian Fault (NAF; Turkey) from the continuous records of the 73 stations of the DANA temporary array in the frequency band 0.1 - 0.5 Hz. The region covered by the stations has rapidly varying geological characteristics and is highly faulted around the northern strand of the NAF. We measured in the noise correlations the space-time evolution of the energy of the coda waves. We first perform measurements in separate sub-regions. The local scattering and attenuation properties are obtained by global optimization of a 2-D solution of the radiative transfer equation for surface waves. We found that the mean free path and attenuation coefficient are considerably varying laterally with strong scattering observed in the region lying along the northern strand of NAF. The optimization provides well-constrained values for the scattering mean free path (ℓ) on the order of 10km in the fault region. The mean free path is much larger (>100km) in the neighboring regions. We compare our global observations with simulations of scattered energy in a laterally variable scattering model using 2-D radiative transfer. These simulations confirm the large contrast of heterogeneity between NAF and the surrounding crust and provide further constraints on the lateral extent of NAF. When sources are located inside the fault zone, we find that energy leakage controls the spatio-temporal distribution of coda wave energy in the medium. This in turn suggests that lateral variations of scattering properties should be taken into account in future monitoring studies.

1 Introduction

After the pioneering works of Aki (1969), it has been widely accepted that the coda of seismic records is composed of waves scattered by heterogeneities in the lithosphere. Aki and Chouet (1975) proposed to describe the energy decay in the coda as a combination of an algebraic and an exponential component. The latter is quantified by a frequency dependent inverse coda quality factor Q_c^{-1} (Aki & Chouet, 1975) and varies with the tectonic style of the region where it is measured (Singh & Herrmann, 1983). The en-

ergy decay in the coda has since then been widely used to extract empirical information on the attenuation properties of the medium (Fehler & Sato, 2003). In spite of this success, it has become clear that precise information of the level of scattering cannot be obtained from the coda decay alone. Based on analytical solutions of the diffusion model in a half-space geometry, it has been proposed that Q_c^{-1} should be close to Q_i^{-1}, the intrinsic quality factor of the crust (Aki & Chouet, 1975). However, Calvet and Margerin (2013) show that even in this simple geometry Q_c^{-1} and Q_i^{-1} only agree when scattering is not too strongly anisotropic and at sufficiently large lapse-time. To properly assess the statistical properties of heterogeneities, and thereby extract detailed information on the Earth's structure and composition, one needs to quantify and distinguish between the intrinsic coefficient Q_i^{-1} and the scattering coefficient Q_{sc}^{-1}, both of them contributing to Q_c^{-1} through a relation that cannot be established in general.

One phenomenological method to investigate the relationship between the observed seismogram envelopes and the spectral structure of the random heterogeneity of the Earth is based on the scalar radiative transfer equation (RTE) (e.g. Hoshiba, 1991, 1993, 1994; Margerin, Campillo, & Tiggelen, 1998; Sato, Nakahara, & Ohtake, 1997; Wu, 1985; Wu & Aki, 1988). In the case of a multiple-scattering medium there are two important parameters that describe the heterogeneity: the scattering mean free path ℓ and the transport mean free path ℓ^*. ℓ, the reciprocal of the scattering coefficient, represents the average distance between two scattering events. ℓ^* is the propagation distance required for a wave to lose memory of its initial direction. The first study taking multiple scattering into account to estimate the relative contribution between scattering and intrinsic absorption was by Wu (1985). The work was based on a stationary transport equation. Later, time-dependent radiative transfer theory has been introduced to describe energy propagation in randomly inhomogeneous media (Sato, 1993a; Shang & Gao, 1988). The first Monte-Carlo simulations using radiative transfer for envelope synthesis were developed in parallel (e.g. Abubakirov & Gusev, 1990; Gusev & Abubakirov, 1987). Hoshiba, Sato, and Fehler (1991) and Fehler, Hoshiba, Sato, and Obara (1992) analysed the entire S-seismogram envelopes (including the ballistic wave) to measure the ratio of scattering attenuation and intrinsic attenuation quantitatively. Their method, known as the multiple lapse-time window analysis (MLTWA), has lead to a large number of studies reporting regional values of the scattering properties (e.g. Mayeda, Koyanagi, Hoshiba, Aki, and Zeng (1992) in Hawaii, Long Valley and Central California; Hoshiba (1993) in

Japan; Jin, Mayeda, Adams, and Aki (1994) in Southern California; Carcolé and Sato (2010) using the Hi-Net stations in Japan). Sato (2019) provides a comprehensive review of scattering mean free paths measurements from rock sample to lithospheric scales. The majority of the these studies use earthquake records of local earthquakes with magnitudes large enough for evaluating coda properties at large lapse times. This limits the spatial coverage and therefore provides average or regional values of scattering properties instead of more specific local values.

Ambient noise cross-correlations (e.g. Shapiro & Campillo, 2004) offer an attractive alternative to study the attenuation parameters on a more local scale, particularly in the lower frequency bands ($f < 1$ Hz). From scattering theory we know that we can reconstruct the Green's function between two stations if we correlate the coda of an impulse source, such as an earthquake (Campillo & Paul, 2003). Furthermore, it has been shown that we can use the coda of correlations to also reconstruct the Green's functions (Stehly, Campillo, Froment, & Weaver, 2008). This is a good indication that the coda of correlations is analogous to the earthquake coda and contains valuable information on the propagation properties.

Wegler and Sens-Schönfelder (2007) were the first to estimate the coda attenuation Q_c^{-1} from ambient noise auto-correlations in Japan. More recently, Soergel et al. (2020) mapped Q_c in the greater alpine region using ambient noise records in the 2.5-20s period band and found large spatial variations of coda attenuation related to the geology. Hirose, Nakahara, and Nishimura (2019) demonstrated that cross-correlations functions (CCF) can be used to derive scattering properties by comparison with active shot data. In their study they derived average scattering properties at the Sakurajima volcano in Japan by minimising the misfit between the energy densities measured in CCFs and the predictions of scalar RTE. Motivated by these recent results, we use the coda of ambient noise CCFs to detect and quantify possible lateral variations of scattering properties across the North Anatolian Fault Zone. Although the mapping of these spatial variations of attenuation across the fault is interesting in its own right, it may also have some important implications for the accurate location of velocity changes based on coda wave interferometry (CWI). Indeed, geological and geophysical studies (see e.g. Ben-Zion & Sammis, 2003, for a review) suggest that the assumption of homogeneous scattering properties underlying most CWI tomographic studies may well break down near fault zones.
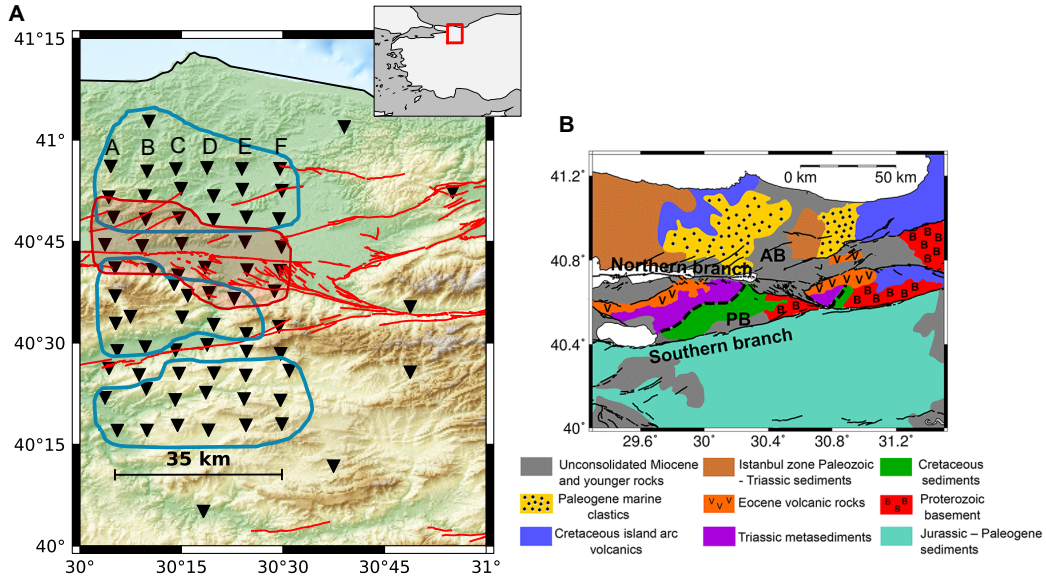
Figure 1. A) Map of the study region showing the DANA network (black triangles) and the main faults (red). The four sub-regions used in the data analysis are delimited by red lines for the fault zone and blue lines for the surrounding crust. The array is composed of 6 columns of stations, labeled a to f from west to east. Each column comprises 11 stations, numbered 1 to 11 from south to north. B) Geological map of the the wider study region (from Taylor et al. (2019)). The Adapazari and Pamukova basin, are indicated by AB and PB, respectively.

Our study area is the North Anatolian Fault Zone (NAFZ; Turkey). This is a seismically active fault zone formed where the Anatolian block and the Eurasian continent meet. The ∼1200km long dextral strike-slip fault has an east-west orientation. The region around the Izmit rupture zone is the area we are considering in current work (see Figure 1). Here the NAFZ splays into a northern and southern strand; separating the study region into the Istanbul Zone in the north, the Armutlu Block in the centre and the Sakarya Zone in the south. The Istanbul zone consists of old and stiff continental material and a deep sedimentary basin, the Adapazari Basin (Şengör et al., 2005). The central block mainly comprises the Armutlu Mountains and has a small sedimentary basin in the southern part constrained by the southern strand of the NAF. The southern most part of our study region is the Sakarya Terrance. Similar to the central block it consists mainly of metamorphic rocks (Okay & Tüysüz, 1999; Yılmaz, Genç, Yiğitbaş, Bozcu, & Yılmaz, 1995). The northern strand of the NAF will be referred to as 'fault zone' (FZ)

in this study, because it has a wider faulted zone than the southern strand, due to the additional small normal faults.

The manuscript consists of two main parts. In the first part, we estimate the spatial variation of intrinsic attenuation Q_i^{-1} and scattering mean free path ℓ from ambient noise cross-correlations (Section 3) using a data regionalization approach guided by geological considerations. In the second part we validate the inferred scattering properties by direct comparison between the data and results of Monte Carlo simulations in media with laterally varying mean free path and intrinsic attenuation (Section 4). The next section is devoted to the description of the data set and signal processing.

2 Data processing and decay properties of coda waves

In this section, we describe the basic processing applied to the data. We show that the coda can be effectively reconstructed and perform an empirical analysis of its decay properties.
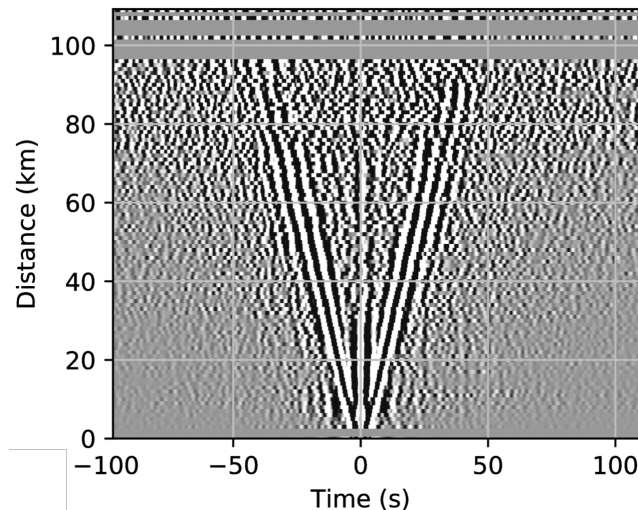
2.1 Data pre-processing

Figure 2. Cross-correlations between all pairs of N-components recorded at DANA in the 0.1-0.5Hz frequency band. The dominant arrivals show energy propagating at velocities that are typical of surface waves.

In this study we exploit ambient noise records from the Dense Array for North Anatolia (DANA (2012); see Figure 1). This array consists of 73 three-component broadband stations, 63 of which are forming a rectangle covering an area of approximately 35 by 70 km with an average inter-station distance of 7 km. The body wave reflection study by Taylor, Rost, and Houseman (2016) and the surface wave tomography by Taylor et al. (2019) provide convincing evidence that microseismic noise can be used successfully at frequencies lower than 1Hz to reconstruct empirical Green's functions from autocorrelations and CCFs with the DANA array. To extract the direct Rayleigh wave and its coda with sufficient signal-to-noise ratio, we computed CCFs using the complete 18 months of continuous data which were recorded during the period between May 2012 and October 2013. The continuous data were first divided into one-hour segments. All components were down-sampled to 25 Hz and corrected for the instrument response before removing segments containing earthquakes of magnitude ≤ 2 as inferred from a local catalog (Poyraz et al., 2015). A spectral whitening was applied to the data between 0.01 and 1 Hz, followed by 4th-order zero-phase Butterworth filtering in the 0.1-0.5Hz frequency band. One-bit normalisation is the last step of the pre-processing and was applied to remove any remaining transient signal. We computed the full cross-correlation tensor between all pairs of stations using 1h windows of pre-processed data. For each station pair, the results from all windows were subsequently stacked to obtain the mean CCFs over the full acquisition period.

Figure 2 shows an example of the resulting CCFs for the averaged horizontal component pairs (for all 9 separate component pairs, see Figure 1 in Supplementary Material). From the first arrivals we derive a velocity, which is approximately equal to 2.1 km/s, indicating that the main energy pulse is most likely composed of surface waves. Henceforth, we will assume the coda to be mostly composed of scattered surface waves. For the short inter-station distances, it is hard to differentiate between Rayleigh and Love waves. This observation is confirmed by the surface wave tomography Taylor et al. (2019), who show that the average velocities of Love and Rayleigh waves are very similar over the study area in the 0.1-0.5Hz frequency band. To verify convergence of the calculated CCFs we compare in Figure 3 the envelopes of CCFs derived from 12 months of stacked data versus 18 months of stacked data. In the coda window the differences are negligible and we are thus confident that our CCFs have converged. The later part of the en-

164 velopes however, are different, showing that the noise levels are not the same across the
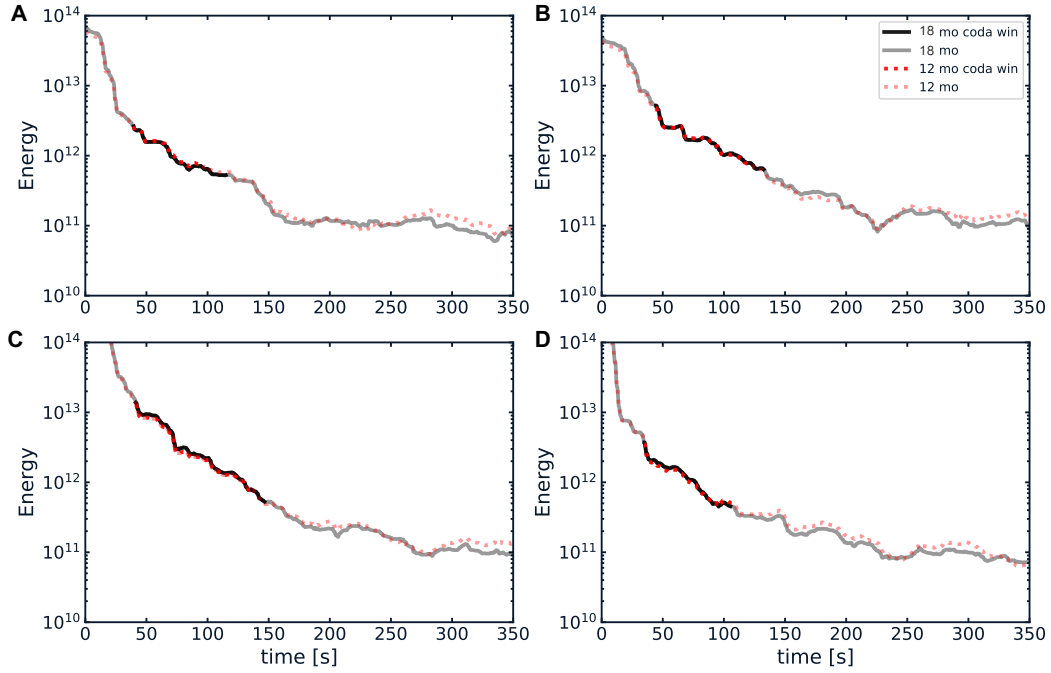
165 study area.

Figure 3. Envelopes of ambient noise cross-correlations obtained by stacking 12 months of data (red dotted line) versus 18 months of data (solid black line). The transparency of the curves is adjusted to delimit different portions of the data. The intense red and black part indicates the coda window, preceded by ballistic waves and followed by noise (high transparency). The four panels correspond to a representative sample of station pairs across the array.

166 ## 2.2 Measurement of Coda attenuation Q_c^{-1}

A first estimate of seismic wave attenuation in Earth's crust underneath the DANA array can be empirically obtained by measuring the energy decay of coda waves. Following Aki and Chouet (1975), we assume that the energy envelopes of noise CCFs obey the same algebro-exponential decay as earthquake data:

$$E(f,t) = S(f) \ \exp[-2\pi \ t \ f \ Q_c^{-1}(f)] \ t^{-\alpha} \tag{1}$$

167 where $E(f,t)$ is the mean-squared energy envelope at lapse time t around frequency f,

168 $S(f)$ is a frequency-dependent factor combining the virtual source magnitude and the

169 site effect at the station and α is an exponent to be discussed below. $E(f,t)$ is obtained

–8–

170 by applying a smoothing window of 16 periods to the squared CCF, which is sufficient

171 to remove rapid fluctuations of the envelope. To further improve the stability of the mea-

172 surements, we subsequently average all four horizontal components of the energy envelopes

173 of the cross-correlation tensor after a normalization of each term has been performed at

174 a fixed lapse-time of 100s. The exponent α is a fixed parameter that depends on both

175 the regime of scattering (from single scattering to diffusion) and the dominant wave type

176 in the coda (body waves or surface waves). It typically varies between 1 and 2. Assum-

177 ing that the ballistic and coda waves are mostly composed of surface waves, we choose

178 α=1. It is worth noting that in 2-D scattering media, the theoretical algebraic decay of

179 energy is of the form t^{-1} in both the single-scattering and multiple-scattering regimes

180 (Paasschens, 1997). Like in previous studies (Soergel et al., 2020), we estimate Q_c^{-1} di-

181 rectly from the slope of the Log-Energy decay of the envelope against lapse time t with

182 a linear least-squares method. We found that the assumption $\alpha = 1$ provides more sta-

183 ble measurements of Q_c^{-1} than higher values ($\alpha = 1.5$ or $\alpha = 2$). We note that the

184 quality of the coda reconstruction is not uniform over the network. In particular, sta-

185 tions located in the south of the array show generally lower S/N ratios. To avoid under-

186 estimation of the decay rate due to noise contamination, we decided to adapt the du-

187 ration of the measurement window to the quality of the CCF. The coda typically starts

188 25s after the ballistic arrival and ends when the signal to noise ratio (S/N) drops below

189 5. We reject all CCFs for which (1) the coda duration is less than 75s or (2) the corre-

190 lation coefficient of the linear regression R^2 is less than 0.75. This provides us with good

191 quality estimates of Q_c^{-1} for the relatively early part of the coda. About ∼55% of the

192 constructed CCFs pass the selection criteria, leading to 1328 Q_c^{-1} measurements. We

193 note that this amount of Q_c^{-1} measurements is for a maximum interstation distance of

194 35 km (for details see next section).

2.3 Mapping of lateral variations of Q_c^{-1}

196 To facilitate the discussion of the results, the inter-station measurements of Q_c in

197 the 0.1-0.5 Hz frequency band have been converted to 2-D maps. The study area is first

198 discretized onto a grid of (∼8.5km-by-12km) pixels. At each pixel, we identify all the inter-

199 station paths of total length smaller than 35km that propagate through and record the

200 corresponding values of Q_c^{-1}. We then estimate the local value of Q_c^{-1} and its uncertainty

201 by computing the arithmetic average of the recorded Q_c^{-1} values and their standard de-
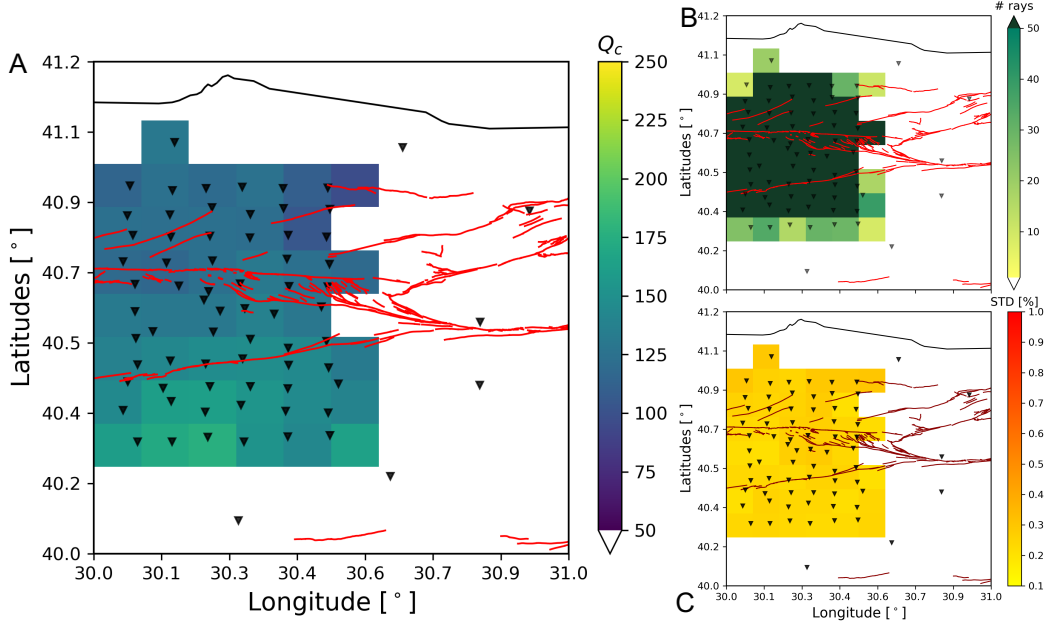
Figure 4. A) Q_c map for causal part of CCFs composed of the averaged horizontal components. It shows the arithmetic mean of Q_c for all rays that cross the cell with a minimum of 5 rays. B) ray coverage for averaged horizontal components C) standard deviation per cell in percentage of the measured Q_c.

viation. The choice of maximum path length (35 km) avoids mixing different propagation regimes and provides a fine spatial resolution. The number of interstation paths per cell are displayed in Figure 4B. There are typically more than 50 rays crossing each pixel at the center of the array which ensures that the features shown on the map are reliable. In SM 2, we show that maps derived from both causal and acausal parts of different component combinations are very similar. Figure 4 illustrates that Q_c is relatively uniform over the entire study region. In particular, the fault zone does not distinguish itself from the surrounding crust. From this negative result, we may be tempted to conclude that the attenuation properties are uniform across DANA. This is not the case, however, as indicated by the direct observations of energy propagation presented below.

2.4 Laterally varying propagation properties

To give a direct image of the propagation properties of the region, and to detect potential local differences in properties, we have represented the energy distribution at different times deduced from the envelopes of the correlation functions. We considered

216   virtual sources located in two very different geological contexts. The first source is lo-

217   cated at the very south of the network (station DA01, Figure 5A) while the second is

218   located in the immediate vicinity of the northern branch of the fault (station DA07, Fig-

219   ure 5B). We measured the energy on non-normalised CCFs between these stations and

220   all others stations of the array. The energy is averaged for all horizontal components in

221   8 different time windows of 30 seconds, between 5 and 75 seconds. The energy snapshots

222   are presented in Figure 5 after temporal correction by the average Q_c . For a source south

223   of the fault system, Figure 5A does not show any spatial pattern after the initial flow

224   of energy from the source. The energy distribution exhibits a speckle-like behaviour, with-

225   out indication of any energy being concentrated at a particular location. On the con-

226   trary, when the source is close to the main fault, Figure 5B shows that the energy is not

227   spread uniformly but that is higher inside the fault zone, especially in the eastern side,

228   than outside the fault zone for lapse times between 25 and 65s. The absence of such a

229   pattern for the source in the south (Figure 5A) indicates that the energy concentration

230   observed in Figure 5B along the northern strand cannot be explained by a local effect

231   such as an amplification due to a shallow structure. One may notice that the region where

232   we find the energy concentration is close to a kink of the main fault where intense frac-

233   turing is expected (King, 1986) and observed (Figure 1). A dense fracture network would

234   result in a strong scattering strength for seismic waves. No clear energy concentration

235   is found for the scenario with a virtual source in the vicinity of the southern branch of

236   the fault zone.   These direct observations suggest specific propagation characteristics

237   along the northern branch that are not revealed by Q_c mapping. In the following, we

238   rely on the Multiple Lapse Time Window Analysis (Fehler et al., 1992; Hirose et al., 2019)

239   to evaluate quantitatively the scattering and absorption properties in different sub-regions.
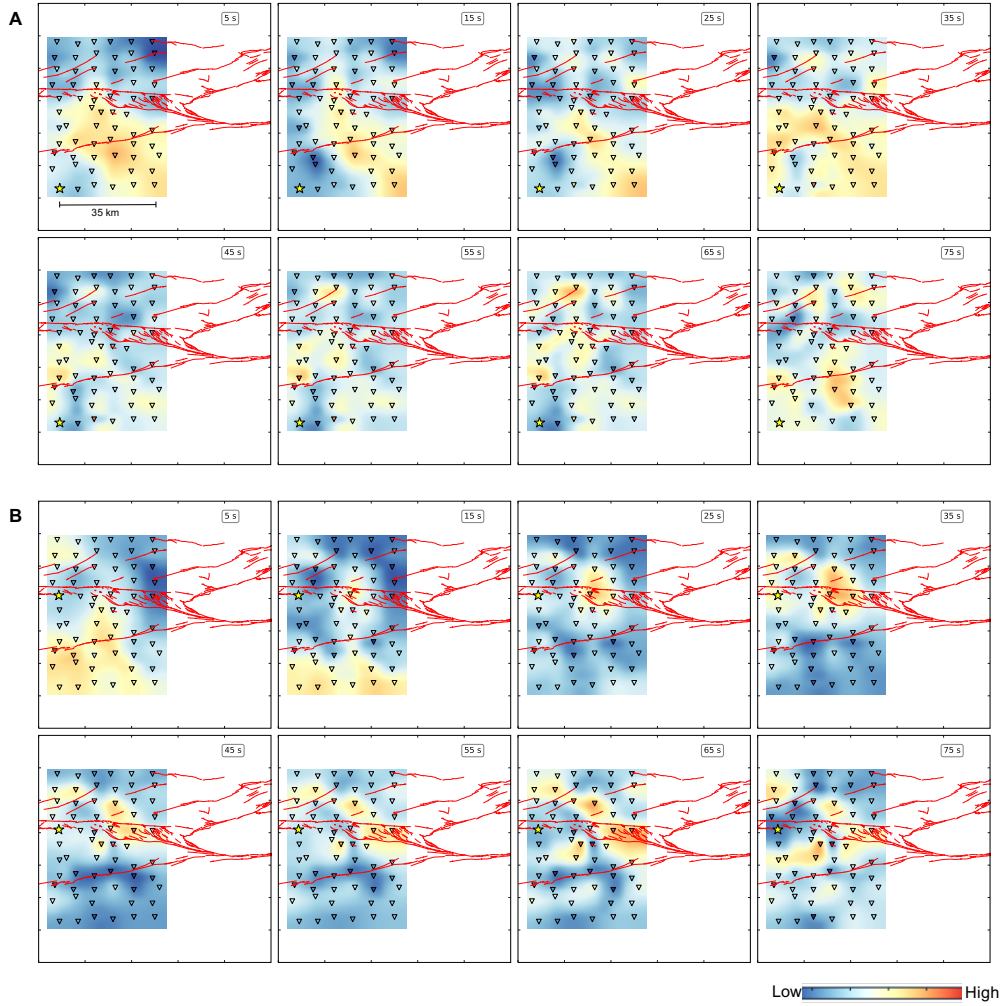
Figure 5. Snapshot of seismic energy distribution derived from ambient noise cross-correlations. The energy values have normalised for display purposes only. Assuming an average coda-Q of 150 in the study area and an average frequency of 0.3 Hz, the energy per time window is multiplied by $e^{2\pi ft/Q_c}$. A) The virtual source is located in the south at station DA01. B) The virtual source station DA07 (depicted by a yellow star) is located inside the fault zone. The color map indicates the energy intensity. Energy is entrapped in the eastern part of the fault zone up until 65s.

3 Mapping of attenuation properties

3.1 Transport model and inversion strategy

As stated in introduction, the attenuation properties of the medium as quantified by the intrinsic attenuation Q_i^{-1} and the scattering mean free path ℓ, are related to Q_c

via an unknown non-linear function. Although the previous section did not reveal significant variations of coda-Q over the region, it does not imply that the scattering properties may not be variable. Since Q_c^{-1} especially relies on the assumption of a simple linear decay of the Log-Energy in the time domain, it may be insensitive to finer details of the spatio-temporal distribution of energy, particularly at small spatial scales. To assess the possible contrasts in scattering properties between the fault and the surrounding crust, we choose to split the study area into four sub-regions where we measure the scattering properties separately. We will refer to the sub-regions as North, 'Fault Zone' (FZ), Centre and South, following a self-explanatory naming convention (see also Figure 1). The definition of each sub-region results from a compromise between the following criteria. A sub-region should be: (1) small enough to ensure some homogeneity in the geology and therefore in the scattering properties; (2) large enough so that the aperture of the sub-array enables reasonable estimates of the scattering properties as further discussed below. We note that the selected stations in each sub-region lie inside the closed curves shown in Figure 1.

To estimate the local scattering parameters we perform a Multiple Lapse Time Window Analysis (MLTWA) as originally proposed for earthquake data by Fehler et al. (1992) and recently applied to ambient noise CCFs by Hirose et al. (2019). In the case of the DANA data, we measure the total energy of the four horizontal components of the CC tensor in four 15-s long time windows starting at 5s, 25s, 50s and 75s after the ballistic arrival. The energy in a late time window of 15s duration starting at lapse-time $t = 100$s is used to normalize the measurements for the magnitude of the virtual sources and the site effects. The observed normalised energy densities (NEDs), E_{obs}, are then averaged in bins of width 2kms, in order to avoid bias towards one specific distance. The spatio-temporal distribution of NEDs in the four sub-regions is shown in Figure 6. It is apparent that the spatial energy decay in the first time window is much faster inside the FZ than outside, which suggests a contrast of attenuation properties between the FZ and its environment. To confirm this interpretation, we infer the values of the scattering mean free path ℓ and the intrinsic quality factor Q_i in each sub-region by comparing the observed NEDs to the predictions of a 2-D radiative transfer equation (RTE) applied to
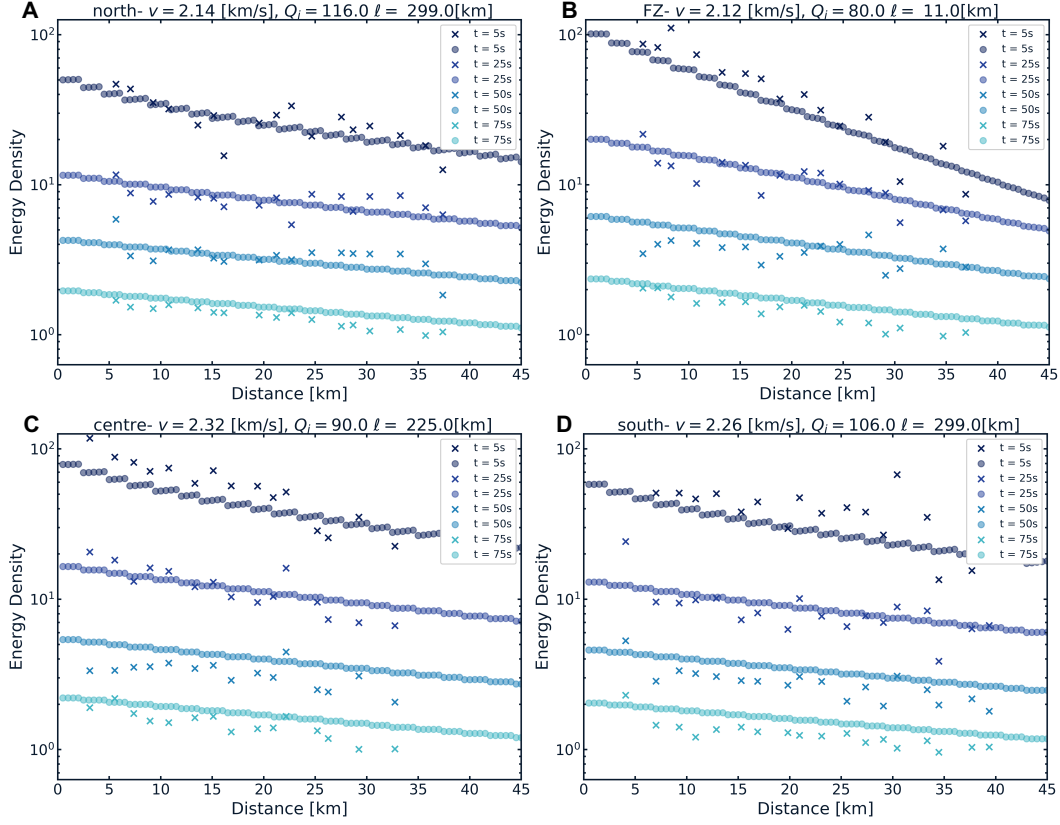
Figure 6. Normalised energy density (NED) in four sub-regions located inside the FZ (B) and outside the FZ (A, C, D). Crosses show the observed NED('x') and circles ('o') the NEDs modelled by the 2-D RTE using the best fitting parameters indicated at the top of each plot. The color correspond to four time windows, with lighter blue colors for increasing lapse times (5s, 25s, 50s, and 75s after the ballistic waves).

the transport of surface waves (Paasschens, 1997; Sato, 1993b):

$$
\begin{aligned}
P(r,t) = & \frac{e^{-ct/l-\omega t/Q_i}}{2\pi r}\delta(ct-r) \\
& + \frac{1}{2\pi lct}\left(1-\frac{r^2}{t^2c^2}\right)^{-1/2}\exp\left[l^{-1}(\sqrt{c^2t^2-r^2}-ct)-\omega t/Q_i\right]\mathcal{H}(ct-r)
\end{aligned}
\tag{2}
$$

259   In Eq. (2), $P(r,t)$ represents the energy density at hypocentral distance r and lapse time

260   t, for energy traveling at velocity c. The symbols $\delta(x)$ and $\mathcal{H}(x)$ represent, respectively,

261   the Dirac delta function and the Heaviside step function. The first term on the RHS of

262   Eq. (2) represents the direct wave contribution and is non zero only at $t = c/r$. The

263   second term models the diffuse energy forming the coda for $t > c/r$. Note that the de-

264   pendence of the intrinsic quality factor Q_i and the scattering mean free path ℓ (and in

265 turn of the energy density P) on the central frequency of the signal ($f = \omega/2\pi$) is im-

266 plicit.

To quantify the agreement between the observed and simulated NEDs, we intro-
duce the following misfit function:

$$SM = \sum_{i=1}^{4} \sum_{j=1}^{M} \left[\log \left(\frac{E_{RTE}(t_i, j)}{E_{obs}(t_i, j)} \right) \right]^2 \qquad (3)$$

267 where E_{RTE} denotes the energy density predicted by the 2-D transport model and the

268 indices i, j refer respectively to the time window and the hypocentral distance bins. Note

269 that the same normalization procedure is applied to the observed and modeled energy

270 densities. In Eq. (3) the logarithm makes sure that all epicentral distances and lapse-

271 time contribute equally to the misfit. To find the optimal value of mean free path and

272 intrinsic attenuation, we perform a similar grid search as in Hirose et al. (2019) and Fehler

273 et al. (1992). The search range for ℓ and Q_i^{-1} is the same for all sub-regions with ℓ vary-

274 ing between 5 and 300 km with increments of 1 km and Q_i varying between 60 and 200

275 with increments of 2. Before discussing the inversion results in the next section we briefly

276 recall why separation of scattering and absorption properties is made possible by MLTWA.

277 The basic ideas were presented in Fehler et al. (1992) but we may revisit their ar-

278 guments in the light of the sensitivity analysis of Mayor, Margerin, and Calvet (2014)

279 which discuss the effect of local perturbations of attenuation properties. These authors

280 show in particular the drastically different impact of scattering vs absorption on the seis-

281 mogram energy envelopes. Scattering mostly affects the amplitude of ballistic waves and

282 the early coda. If the scattering perturbation is located on the direct ray connecting the

283 source and station, energy is removed from the direct waves and redistributed at later

284 time in the coda. By contrast, a perturbation of absorption has a uniform impact on the

285 energy envelop and affects the overall rate of decay of the energy in the time domain.

286 For more complicated scenarios (e.g. scattering perturbation located off the direct ray),

287 we refer to (Mayor et al., 2014). The fact that different time windows of the signal have

288 quantitatively distinct sensitivities to elastic and anelastic perturbations is the key to

289 MLTWA.

3.2 Inversion results: absorption (Q_i^{-1}) and scattering (l).

291 Figures 6 and 7 show the results of the optimization procedure for the scattering

292 mean free path and the intrinsic absorption in each sub-region. The comparison of the
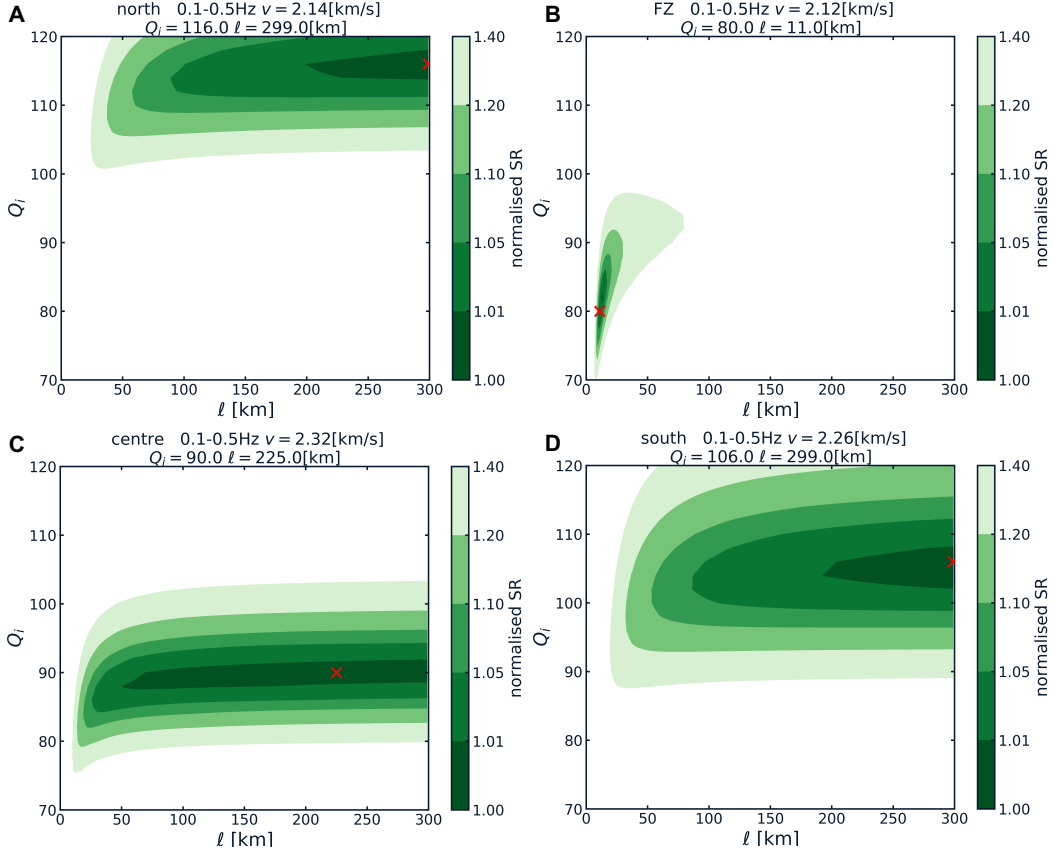
Figure 7. Resulting misfit and optimal values for the grid search in the 4 sub-regions. A), C) and D) for the regions outside the FZ, north, centre and south respectively; B) for inside the FZ. The green color indicates the values of normalised sum of the misfit (SM; as in Eq. 3), with the darkest color for the smallest misfit. The values are normalised w.r.t. the minimum SM. The best fitting values are indicated by the red crosses ('X').

predictions of the best-fitting model with the data indicates that a simple 2-D RTE is sufficient to capture the general spatio-temporal energy distribution across DANA, provided that different attenuation parameters are employed in different sub-regions (see Figure 6). We first discuss the inversion results in the FZ. We note that the level curves of the misfit function in the $\ell - Q_i$ plane shown in Figure7B indicate well-constrained values for ℓ of the order of 11km and $Q_i \approx 80$, assuming a group velocity of 2.1 km/s deduced from the surface wave arrival times in the sub-region. The most outstanding observation which is reproduced by the RTE-model is the rapid spatial energy decay inside the fault zone, mainly visible in the earliest time window of Figure 6. Compared to typical values reported in the literature (Sato, 2019), a scattering mean free path of the

order of 10 km is rather small. Yet it is still larger than the dominant wavelength of surface waves so that localization effects (see e.g. Hu, Strybulevych, Page, Skipetrov, & van Tiggelen, 2008) are probably negligible and the use of a transport model is legitimate. It is worth emphasizing that a scattering mean free path of 10km is not common in Earth's crust. Although comparisons with earthquake data are not straightforward due to the difference in frequency bands, comprehensive studies by Carcolé and Sato (2010) in Japan or Eulenfeld and Wegler (2017) in the United States suggest generally larger values of the order of 100kms or more. The level of absorption ($Q_i \approx 80$) is also found to be rather low but not exceptional for the sub-surface of the Earth. For the southern strand of the NAF we also performed the inversion, but no significant difference in neither the spatial decay rate nor the resulting ℓ and Q_i were observed compared to the neighboring central and southern sub-regions.

In the neighboring sub-regions, Q_i is well-constrained and the best-fitting values are slightly higher than inside the fault zone with $Q_i \approx 116, 90, 106$ for the north, centre and south respectively. However, within a 20% error range Q_i shows similar values inside and outside the FZ and typically ranges between 80 and 120. From north to south, the surface wave velocity used in the simulations is 2.1km/s, 2.3km/s and 2.3 km/s, again derived from the arrival time of the direct waves. The values of Q_i are generally not consistent with the estimates of Q_c, as we would have expected the reversed trend with higher Q_i values in the south than in the north. This discrepancy may again be purely a consequence of the generally more complicated envelope shape of the data than the simple parametric form of the decay underlying Q_c measurements. The misfit contours of Figure7 show that the mean free path is less well constrained outside the fault zone than inside. This is not surprising, as the mean free path ($\ell \geq 40$km) appears to be of the same size or larger than the largest linear dimension of the sub-network. The 20% error range indicates ℓ may range from 40km to over 300 km (300 km is the maximum value tested) in the normal crust. These values are typical of what is found worldwide (Carcolé & Sato, 2010; Eulenfeld & Wegler, 2017; Sato, 2019).

3.3 Effect of Velocity Model and Noise

To asses the robustness of the optimization method and to better understand the poorer constraint on ℓ we explore the effect of the surface wave velocity and of the 'noise' in the data. For all four sub-regions different velocities are used, because they are de-

rived from the first arrival estimates per sub-zone. Similar to the Rayleigh wave tomography results of Taylor et al. (2019), we found the highest velocities in the centre and the lowest in the north. The actual values of the velocities, however, may be slightly different from the ones we derived via the first arrival estimate, which affects the optimization. Although marginally better fits (smaller SMs) are obtained when using lower velocities in all sub-regions, there is no significant effect on the inverted scattering properties (for more details see SM 3.1). Additionally, fluctuations in the NED measurements, or 'noise', affect the optimization and the resulting scattering properties as well. This is especially the case for zones with slow energy decay with distance in combination with a short array aperture. This aspect is also explored in greater details in the SM 3.2. The main findings from this section are that 1) Q_i is always well resolved because Q_i controls the typical energy ratio between the different time windows and 2) ℓ controls the slope of the first time window and may not always be well resolved due to the limited aperture of the array.

4 Completing the cycle: comparing observations with energy transport simulations

To better understand the physical processes that play a role in the spatial and temporal energy propagation in a medium containing inhomogeneously distributed scatterers, we perform Monte-Carlo simulations of 2-D energy transport in a medium with possibly variable ℓ and Q_i. Technical details of the numerical implementation are presented in Appendix A. Comparing the observations with the results from the simulations provides us with insights about the scattering process in the NAFZ.

To facilitate the discussion, we compare two types of models: i) homogeneous models, where the full space has the same scattering properties everywhere (further details may be found in the SM 4.1), and ii) inhomogeneous models, where space is divided into four different sub-regions including a fault zone, each with different scattering properties. The motivations for this heterogeneous model are as follows (1) as discussed in section 3.2, the optimization is performed region by region, consequently there is no guarantee of global agreement between the data and the model, and (2) as we have observed in Figure 6, the fit between the data and the model is not perfect, suggesting that there is room to improve the lateral variations in the model. To maximise the ability to compare the simulations with the observations, we use the same dimensions in the simula-

³⁶⁷ tions as in the study region. However, we halved the inter-station spacing to increase the

³⁶⁸ number of NED measurements in the simulations. This is because we have in total more

³⁶⁹ stations in the actual observations and therefore NEDs for most of the 2km bins.

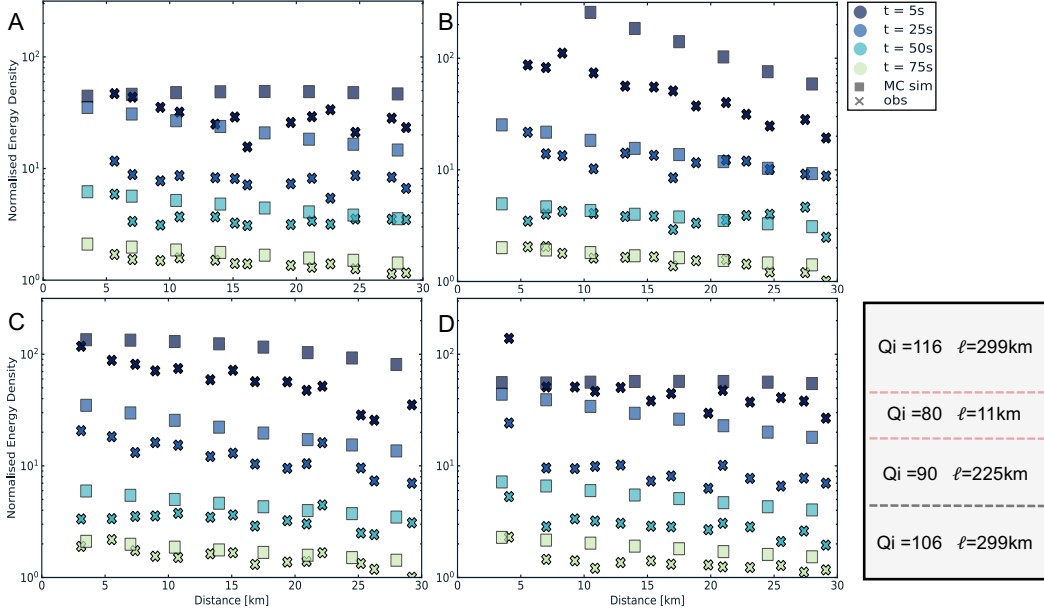³⁷⁰ ### 4.1 Constraints on the fault zone width

Figure 8. Comparison of spatio-temporal energy evolution between observations (crosses) and simulations (squares) for all sub-regions: A) north, B) FZ, C) centre and D) south. The colors indicate the different 15s-long time-windows, starting at 5s, 25s, 50s and 75s respectively. The results correspond to the initial heterogeneous model, based on the scattering properties derived from the regionalization approach and schematically shown in the lower right corner.

³⁷¹ Two different configurations are used for the simulations in the case of inhomoge-

³⁷² neous models. The first configuration has east-west oriented receiver lines. They record

³⁷³ the intensities for sources excited in the corresponding sub-region. An example of this

³⁷⁴ configuration is shown in Figure 9. For these simulations we perform again the MLTW

³⁷⁵ analysis and compare the results with the observations. Figure 8 shows that for all sub-

³⁷⁶ zones and all time windows the NEDs are greater in the simulations than in the obser-

³⁷⁷ vations, especially for the fault zone and the centre at early times. Taking simply the

³⁷⁸ parameters derived in four homogeneous models and combining them in one heteroge-

³⁷⁹ neous model seems insufficient to explain all observations in our study area. We have
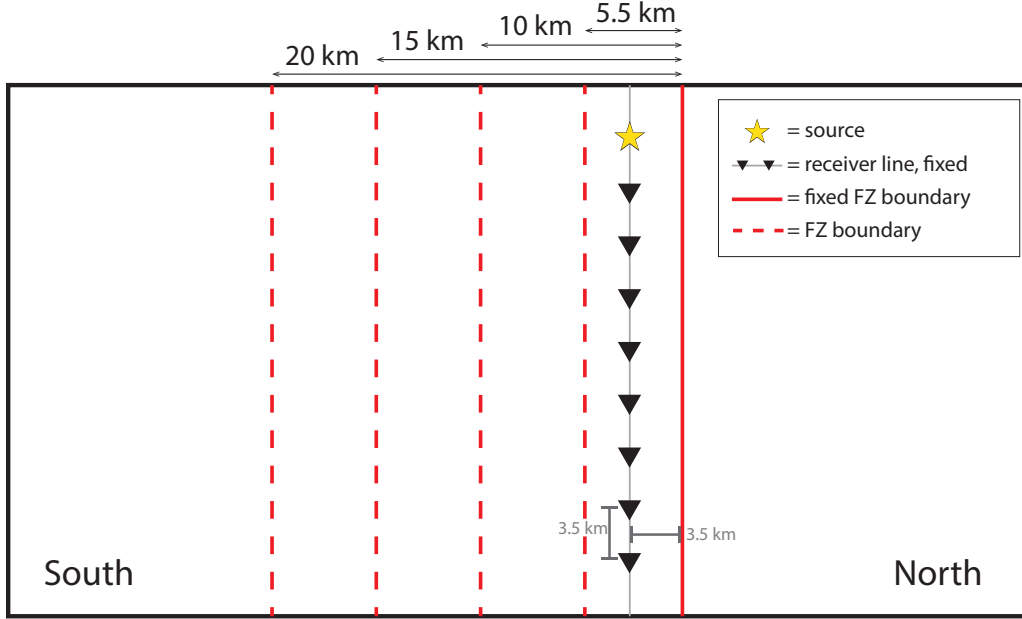
Figure 9. Example of the configuration for the simulations. Depending on the specific case, homogeneous or inhomogeneous, the model is divided in sub-regions where a source and an east-west receiver line is placed with receiver spacing 3.5km. Th specific configuration shown above is used for the inhomogeneous case with different fault zone widths. The different widths are realized by shifting the southern boundary (dashed red line). The fault zone boundary towards the north (right side) is fixed, as is the position of the receiver line w.r.t. the northern boundary and the source.

380 seen in the previous sections that (i) we constrain ℓ inside the FZ but it proved to be
381 more difficult outside, and (ii) there is a clear difference in the decay rate with distance
382 between inside and outside the fault zone (Figure 6). Consequently, the main focus of
383 this section will be on explaining the observations in the fault zone. To simplify the anal-
384 ysis we assume uniform scattering properties outside of the fault zone from here onward.

385   Figure 10 shows four panels with observation and simulation results inside the FZ.
386 We first discuss the simple homogeneous models: panel A for a model space where Q_i
387 =100 and $\ell = 10$ km, and panel B where Q_i =100 and $\ell = 150$ km. Both models do not
388 match the observations to a desirable degree, especially in the first time window. For the
389 model with strong scattering (A), the spatial energy decay in the first time window of
390 the simulations is similar to the observations but the values themselves are too low. For
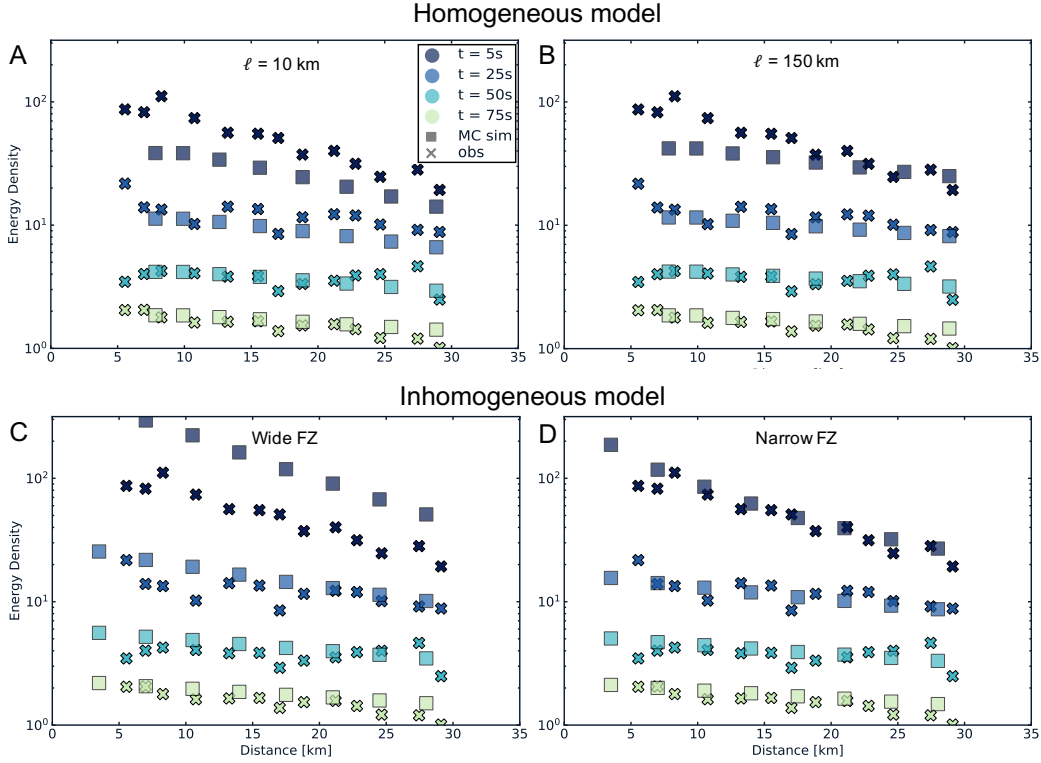
Figure 10. Comparison of spatio-temporal energy evolution between observations (crosses) and simulations (squares) for the FZ only. The upper two panels correspond to simulations in homogeneous models with A) ℓ=10 km and $Q_i = 80$, B) ℓ=150 km and $Q_i = 80$. The lower two panels are for a simple model with $Q_i = 80$ and ℓ=10 km inside the FZ, and $Q_i = 106$ and ℓ=150 km outside the FZ. C) for a wide fault zone, of 14 km and D) for a narrow FZ of 5.5 km. The colors indicate the different 15s wide time windows, starting at 5s, 25s, 50s and 75s respectively.

391   the weaker scattering model (B), it seems the other way around. The decay rate with

392   distance at early times in the simulations is too slow, but the NED values are closer to

393   the observations. Panel C and D show results for a simple heterogeneous model, with

394   inside the FZ Q_i =80 and $\ell = 10$ km, and outside the FZ uniform scattering properties

395   for all sub-zones (Q_i =100 and $\ell = 150$ km). The difference in the models between panel

396   C and D is the width of the FZ, 14km for (C) and 5.5km for (D). Although the results

397   for the wide FZ have the correct energy decay rate with distance, using a narrower zone

398   with strong scattering yields an almost perfect match to the observations. This is in line

399   with the findings of the tomography studies in the region (e.g. Kahraman et al., 2015;

400 Taylor et al., 2016), suggesting a fault zone that is perhaps not wider than 7km down
401 to the mantle.

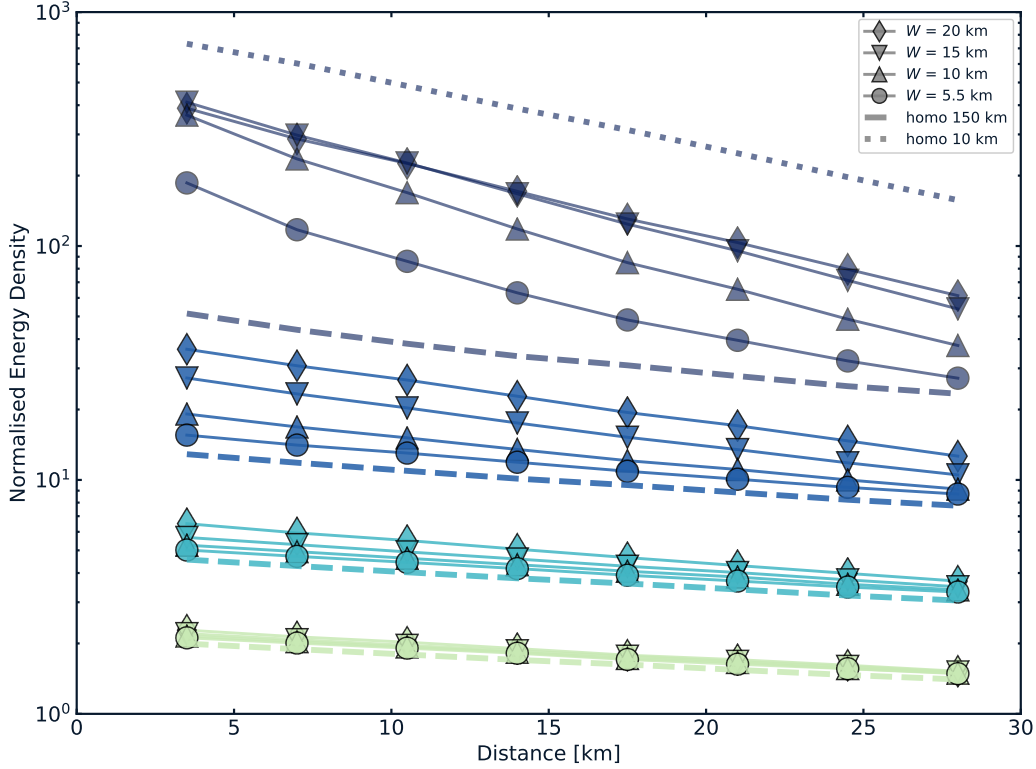402 ## 4.2 The signature of a finite width scattering zone

Figure 11. Comparison of spatio-temporal energy evolution for homogeneous and inhomogeneous simulations with different FZ width. The dashed and dotted lines show NEDs for homogeneous models with ℓ=150 and 10 km, respectively. The NEDs of the inhomogeneous simulations are indicated by the continuous lines and markers, for different widths of the fault zone, W, as indicated in the legend. The colors indicate the different 15s wide time windows, starting at 5s, 25s, 50s and 75s respectively.

403 In the case of a structure with a band of material associated with high scattering
404 taken between regions of low scattering, the energy decay with distance depends not only
405 on the values of ℓ , as we saw in the numerical tests of the previous section, but also on
406 the width of the band. Figure 11 shows the simulation results for fixed values of ℓ (10
407 and 150km) and varying the band width W. We compare the behaviour of heterogeneous
408 models with that of homogeneous models associated with the two values of ℓ 10 and 150km.

409 Note that for the heterogeneous models and the homogeneous model with $\ell =150$km,

410 the energies were normalized by their energy at 100s, as was done in the data analysis.

411 A first observation is that in our time and distance configuration, the heterogeneous mod-

412 els have very similar behaviors at 50s and almost identical at 75s. For the latter time

413 the results are very similar to those of the homogeneous model with $\ell =150$km. A first

414 simple argument is the fact that the area of the strong scattering band becomes small

415 in front of the total area covered by the scattered waves (Figure 9). The results pre-

416 sented here have been normalized to 100s, to be consistent with the MLTWA analysis,

417 but we have verified that the absolute long time energies for the heterogeneous and ho-

418 mogeneous models with $\ell =150$ km are close (see Figure 16 in SM). Their relative dif-

419 ference follows approximately a scaling in W/t, deriving from the same simple geomet-

420 rical argument. We thus observe a convergence towards the solution of the external model

421 with $\ell =150$km for long time in all cases. These results thus indicate that it is difficult

422 to detect a heterogeneity from the observation of temporal decreases at long times, which

423 explains why our characterization with Q_c was in vain.

424   The most important differences between the models are observed for the short times.

425 Let us consider the case of the window starting 5 s after the arrival of the direct waves,

426 which is critical in our comparison with the data. For this time window we have plot-

427 ted in Figure 11 in dotted line the homogeneous model decay with $\ell =10$, the value in

428 the band representing the fault zone. Contrary to the other models and the data, the

429 energies were not normalized with the 100s values for this homogeneous model. Based

430 on our previous conclusions, the normalization was done with the values of the exter-

431 nal homogeneous model ($\ell =150$km) towards which the solutions of the heterogeneous

432 models tend for long times. This normalization is carried out only for interpretation pur-

433 poses, while approaching the data analysis conditions. Indeed, we know that the solu-

434 tions converge towards the homogeneous case with $\ell =150$km, but that they show dif-

435 ferences at finite times (see Figure 16 in SM for non-normalized results). Since the band

436 widths considered are small in relation to the distances travelled by the waves, and the

437 sources are located near the band boundary, a significant portion of the energy escapes

438 rapidly from the central band and will not be subject to intense scattering. Thus, a sig-

439 nificant shift between the curve of the normalized homogeneous model and the hetero-

440 geneous models is observed even from the short distances. For all widths, this shift in-

441 creases with distance, which, it should be remembered, determines the absolute time of

442 the energy measurement window. This can be explained by the decreasing role played

443 by the central band as the surface occupied by the diffracted waves grows, leading to the

444 convergence of the heterogeneous models towards the homogeneous one with $\ell = 150$km

445 for long times. We note that all heterogeneous models exhibit a decay with distance that

446 is larger than the one of the homogeneous $\ell = 10$km model.

447   The amplitude and decay of the normalized energies vary significantly with W. In

448 the case where $W = 5.5$km, that is smaller than ℓ in the band, a significant shift is ob-

449 served with the homogeneous model $\ell = 10$km and the other models at the shortest dis-

450 tance. The curve exhibits first a rapid decrease with distance then approaches the curve

451 of the homogeneous model $\ell = 150$km, a convergence which is observed with the curves

452 of the longer times. The amplitude is explained by the small size of the strongly diffract-

453 ing band (5.5km) with respect to the radius or the region sampled by the waves. Even

454 at the shortest distance, with the time window considered (here between 6.5 and 21.5s),

455 the propagation of the waves is predominantly in the external environment. The posi-

456 tion of the source in the band must also be taken into account when comparing ampli-

457 tudes at short distances for the different geometries.

458   For the other values of W, the same evolution can be observed globally. For $t = 5$s,

459 the curves gradually separate to approach the asymptote at distances increasing with

460 W. The same behavior is observed for the other lapse-times. The evolution of the curves

461 illustrates the transition between two limit models: strong scattering in the band for short

462 times and weak for long times. Note that our configuration does not allow the first regime

463 to be fully observed because the widths for the fault zone are small. The differences be-

464 tween the heterogeneous models diminish rapidly with time or distance and the constraints

465 on the model must be searched in a rather short time range but over a range of distances

466 that covers the characteristic dimension/width of the heterogeneity. If we consider an

467 observation at a fixed distance, e.g. 3 km, the amplitudes for W from 10 to 20 km are

468 very similar for $t = 5$s (the waves sample the same part of the model), much more sep-

469 arated for 25s (at different convergence stages), then again very close for larger lapse-

470 times (close to the asymptote). This example shows the need for a global vision of the

471 behavior and a complete modelling. In particular, the effects of finite size of the diffract-

472 ing band cannot be simply expressed by a single attenuation operator for each pair (W,

473 ℓ) that would apply at all times.

474

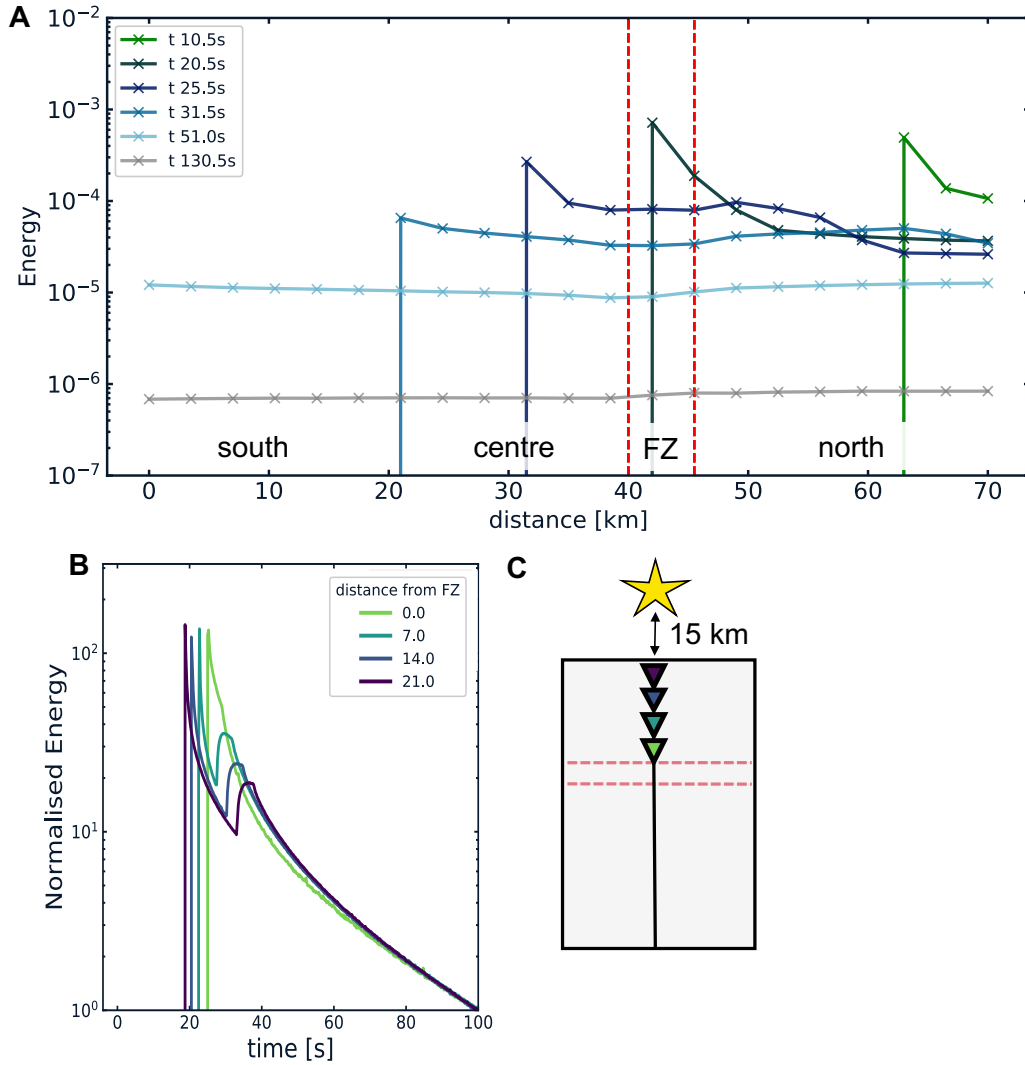## 4.3 Back-scattered Energy from the Fault Zone

Figure 12. A) Snapshots of energy propagation, showing the effect of a strong scattering zone. The graphs show the energy density as function of distance (from right, north, to left, south) at different times. The red dashed lines indicate the fault zone. B) Normalised energy density versus time for four different receivers (7 km apart) in the same simulation. C) Simple heterogeneous model used for the simulation exhibiting a narrow fault zone, with $\ell/W = 2$, $\ell = 10$ km inside the FZ, $\ell' = 150$ km outside the FZ and $Q_i = 100$ everywhere. The receiver line is oriented north-south, in line with the source in the north, 15 km from the first receiver (yellow star). The color scale of the stations (C) and envelopes (B) indicates the distance between the station and the fault zone.
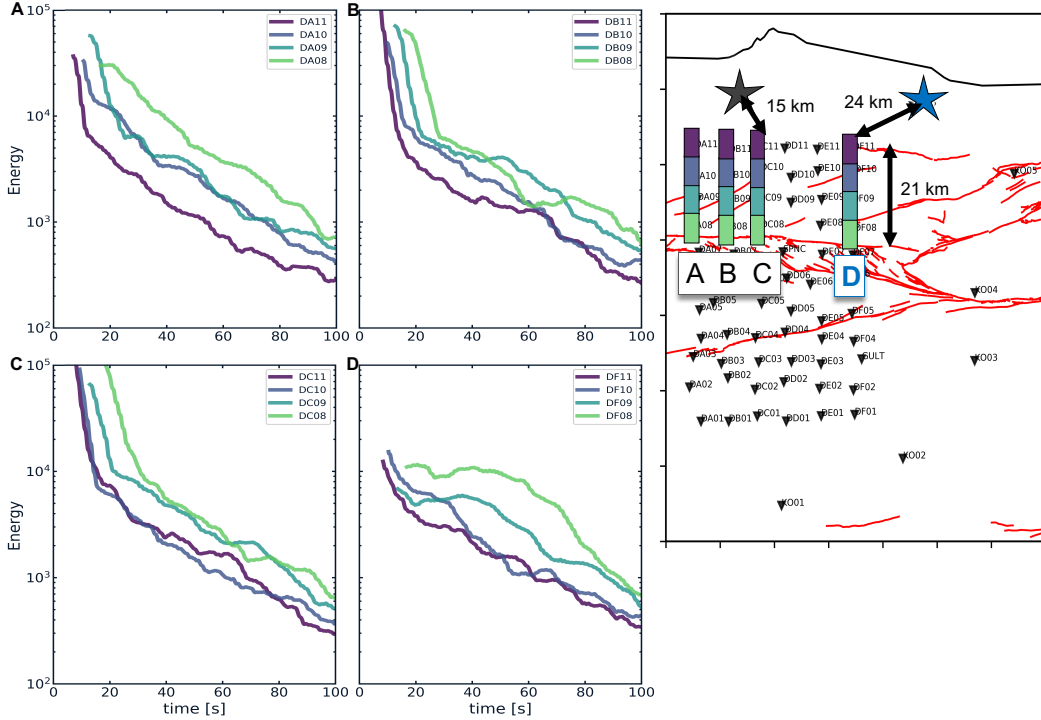
Figure 13. Observations of energy envelopes for station pairs oriented perpendicular to the fault zone. The same color scale as in Figure12B-C is used to indicate the distance between the stations and the fault zone. The map view shows sections A-D. For section A-C, the virtual source is the grey star (permanent station KO07). For section D, the virtual source is the blue star (permanent station KO06). The distance to the virtual sources are indicated on the map. Note: envelopes have been re-scaled with respect to the distance, d, between virtual source and station ($20 \times d$) to enhance the visibility of energy move-out.

In this section we explore the effects of a strong, narrow band of scattering on the energy evolution in space and time. The model we use is the one that seems most optimal from the previous section (with a FZ width, W, of 5.5 km and $\ell = 10$ km inside, and $\ell = 150$ km outside the FZ). The configuration for these simulations is different than previously. The model space is again heterogeneous but the receiver line is north-south oriented. Snapshots of the resulting energy distribution, normalised energy envelopes as a function of lapse-time and the simulation configuration are shown in Figure 12A-C respectively. The most striking feature we observe on both the time-domain envelopes and the snapshots is a 'bump', which can be interpreted as back-scattered energy from the fault zone. When the ballistic energy reaches the fault zone, a front of diffuse energy prop-

agates back towards the direction of the source (Figure 12A). Figure 12B shows the same feature, where for stations farther away from the FZ it is easier to distinguish between ballistic energy and back-scattered energy. As we can see when the station is closest to the FZ, both back-scattered energy and ballistic energy arrive at similar times. At a lapse time of the order of 50s, we observe an inhomogeneous distribution of energy associated with the lateral variations of scattering properties that progressively disappears at long lapse-times (Figure 12A). If this phenomenon of strong back-scattering energy is also present in the actual data, mixture of these energies can have profound implications for the coda decay and scattering properties analysis. Unfortunately, identification of these bumps in the actual CCFs proved to be more difficult than expected.

In the map view of Figure 13 we show four sections (A-D) perpendicular to the fault zone, with a 'virtual source' roughly in line but as far as possible from the stations to accommodate a move-out of this potential back-scattered energy. Sections A-C have permanent station KO07 (grey star) and section D has permanent station KO06 (blue star) as their virtual source. The simulation (Figure 12B) discussed above is most similar to section B of Figure 13. Additionally, the color codes for the envelopes are kept similar. It is expected for the back-scattered energy to arrive later in the stations farther away from the fault zone. Unlike the predictions from the simulations, we fail to observe back-scattered energy in the data (Figure 13). The simple model with a strong narrow band of scattering (Figure 12) seems to make predictions that are to discern in the data. This suggest that the fault zone is far more complex than the simple conceptual model proposed in this paper. Other medium properties such as the density and seismic velocity may be significantly different inside the fault zone versus outside. This can cause a high acoustic impedance contrast and therefore trap energy within the fault zone (Ben-Zion & Sammis, 2003). In our simulations we have not taken other medium properties than attenuation into account. It also seems reasonable to think that there are variations of scattering strength along the strike of the fault. To investigate this possibility, we perform a virtual simulation of energy entrapment in the FZ using the real data.

5 Discussion

5.1 Fault zone trapped energy

As described in Section 2.4, energy seems trapped in the northern strand of the fault, for the case of a virtual source inside the fault zone (Figure 5B). For comparison, no energy entrapment is found for the scenario where the virtual source is in the southern most part of the study area (Figure 5A). The total energy distribution in the fault zone does not correlate with either the surface wave velocities (Taylor et al., 2019) or the earthquakes in the region (catalogue from http://www.koeri.boun.edu.tr/sismo/2/earthquake-catalog/). Additionally, Share, Allam, Ben-Zion, Lin, and Vernon (2019) showed energy entrapment in the San Jacinto fault zone using teleseismic and local earthquakes and a dense linear array along the fault zone. This favors the hypothesis of energy entrapment in the fault zone, and it may partly account for the remaining differences between the observations and simulations in Figure 10D. In the southern branch of the NAF we did not find any entrapped energy. This is in line with the findings mentioned in Section 3.2: the lack of significantly different scattering properties for this branch of the fault zone compared to the surrounding southern region. The absence of both concentrated energy and distinct scattering properties in the southern branch may be explained by the small damage zone, due to the lower activity of this fault (e.g. Aslan et al., 2019).

5.2 Fault zone complexity

We found a strong variation in scattering properties across the fault zone which promotes energy leakage. Evidently, the boundary between the fault zone and the surrounding medium is not purely of scattering properties. Our model, with simple backscattering, provides a first order view but the actual structure is more complicated as observed in the remaining differences between the data and simulations. Effects of other physical quantities such as variations in seismic velocities and waves trapped in the fault zone have potentially a noticeable impact on the spatio-temporal energy evolution too. This corresponds to previous findings in the numerical study of Ben-Zion and Aki (1990), where they found waveform complexities and large amplitude amplifications due to head waves, surface waves and trapped modes in the presence of fault zone material heterogeneity. Additionally, section D in Figure 13 shows anomalies in the coda, compared to the codas of sections A-C. These anomalies in combination with the energy entrapment

towards the east of the fault zone, potentially also suggest along-strike variations. The scattering mean free path may be smaller in certain parts of the fault than anticipated, as well as the width, leading to a more transparent fault zone in certain areas. Furthermore, the more complex fault structure towards the east of the DANA array may leave an imprint on the observed energy distribution.

6 Conclusions

This paper clearly demonstrates that a high scattering limited fault zone needs to be included in a first order model for the DANA region. A narrow fault zone of ∼5.5 km width with a scattering mean free path of the order of 10 km, surrounded by a medium with 150 km scattering mean free path, has been obtained by analysis of ambient noise cross-correlations in the 0.1-0.5 Hz frequency band. We verified that our model reproduces a concentration of energy in the fault zone when the source is inside, as it is visible with the actual data (Figure 5B). This is clearly seen for long lapse times, that is between 35 and 75s, in the simulations presented in SM Figure 17. Currently ambient noise monitoring methods rely on the assumption that scattering properties are the same across fault zones. Here, we have demonstrated that this is not the case. Therefore, laterally varying scattering properties need to be taken into account in future monitoring efforts.

From a methodological perspective we can conclude that one can use the coda of correlations for attenuation studies. More importantly, this study reports for the first time short scale variations in scattering properties. Although we know that scattering properties vary between different types of crust, e.g. between volcanic and normal crust, the derivation of the variations on such short scale has not been reported yet. Our results have direct implications for applications such as monitoring velocity changes in the Earth's crust. Having an estimation of the scattering properties in one's study area can have a significant impact on both the location and the quantity of temporal velocity changes one finds. Future improvement of the model should be focused on incorporating lateral variations along the fault zone, because the data revealed that there is even more complexity than we describe by our model. A larger array, with an extension towards the east, is necessary to capture the complexity.

581   **A Monte-Carlo simulations in laterally varying scattering media.**

582   We remind the reader that Monte-Carlo simulations designate a class of stochas-

583   tic methods of solution of radiative transport equations. In this approach, energy is rep-

584   resented by discrete seismic phonons who undergo a sequence of collisions upon which

585   their direction of propagation changes according to the laws of scattering. In a medium

586   with uniform scattering properties, the distance d between two collisions (also called free

587   path length) is governed by an exponential probability law of the form $p(x < d < x +$

588    $dx) = \ell^{-1}exp(-x/\ell)dx$ with ℓ the scattering mean free path. For greater details, we

589   refer the reader to the literature as summarized in Shearer and Earle (2004) and Sato,

590   Fehler, and Maeda (2012). To simulate the transport of seismic energy in media exhibit-

591   ing spatial variations of scattering and absorption, we have employed the so-called method

592   of null or delta-collisions (Lux & Koblinger, 1991). This is an exact method of simula-

593   tion that maps the transport process from a medium where attenuation properties vary

594   spatially onto a medium where they are constant. Let us remark first that, in the frame-

595   work of Monte-Carlo simulations, absorption may be treated as a scattering process that

596   reduces the energy of a particle by a factor B, with B the local value of the albedo. Hence,

597   to get a grasp on the method it is sufficient to treat the case of inhomogeneous scatter-

598   ing properties, which is also most relevant to our applications.

Consider a 2-D transport equation with a spatially varying mean free path $\ell(\mathbf{r})$.
The equation governing the transport of the energy is (e.g. Paasschens, 1997):

$$(\partial_t + c\mathbf{k} \cdot \nabla + \tau(\mathbf{r})^{-1})e(t,\mathbf{r},\mathbf{k}) = \tau(\mathbf{r})^{-1} \int_{2\pi} p(\mathbf{k},\mathbf{k}')e(t,\mathbf{r},\mathbf{k})dk' \qquad (A.1)$$

with $e(t,\mathbf{r},\mathbf{k})$ the energy density flowing in direction $\mathbf{k}$ (vector on the unit circle) at time
t and position $\mathbf{r}$, $p(\mathbf{k},\mathbf{k}')$ the scattering pattern governing the rate of transition from prop-
agation direction $\mathbf{k}'$ to propagation direction $\mathbf{k}$, c the seismic velocity, and $\tau = c\ell$ the

scattering mean free time. The integral on the left-hand side is over all the directions in the plane. We remark that if $e(t, \mathbf{r}, \mathbf{k})$ solves Eq. (A.1), it also solves the following equation where the effective scattering mean free time τ_e is *constant*:

$$(\partial_t + c\mathbf{k}\cdot\nabla + \tau_e^{-1})e(t, \mathbf{r}, \mathbf{k}) = \tau(\mathbf{r})^{-1}\int_{2\pi} p(\mathbf{k}, \mathbf{k}')e(t, \mathbf{r}, \mathbf{k})dk' + \tau_{nc}(\mathbf{r})^{-1}\int_{2\pi}\delta(\mathbf{k}, \mathbf{k}')e(t, \mathbf{r}, \mathbf{k})dk',$$
(A.2)

where $\delta(\mathbf{k}, \mathbf{k}')$ is the delta function on the unit circle, $\tau_{nc}(\mathbf{r})$ is the scattering mean free time for the null or delta scattering events and $\tau_e^{-1} = \tau(\mathbf{r})^{-1} + \tau_{nc}(\mathbf{r})^{-1}$. In effect, all that we have done is to add the same term $\tau_{nc}(\mathbf{r})^{-1}e(t, \mathbf{r}, \mathbf{k})$ on both sides of Eq. (A.1). But the benefit is in fact immense because in the fictitious medium with null collisions, the scattering mean free path is constant, so that the most basic implementations apply straightforwardly. Note that there is a certain degree of arbitrariness in the definition of τ_e. Assuming that τ is bounded in the domain of interest, we may simply take $\tau_e^{-1} = \sup\tau(\mathbf{r})^{-1}$.

In practice, these ideas may be very easily implemented as follows. The transport process is simulated in a medium where the mean free path $l_e = c\tau_e$ is constant, so that the simple exponential probability law described above still applies. At each collision point $\mathbf{r}_c$, we must decide whether a true or a fictitious scattering event occurs. To carry out this task, we select a uniformly distributed random number in the interval $]0, 1[$ and compare it to the local scattering conversion rate. If:

$$\epsilon < \tau(\mathbf{r}_c)^{-1}/\tau_e^{-1}$$
(A.3)

then a genuine scattering occurs and we proceed as usual with the selection of a new propagation direction. Otherwise, we have a null collision and the propagation direction is unchanged up to the the next collision. The main computational overload comes from the fact that we are in fact simulating more scattering events than actually occur in the real world. But this is largely counter-balanced by the considerable simplification of the free path length selection as well as the absence of complicated geometrical tracking of the particle.

References

Abubakirov, I., & Gusev, A. (1990). Estimation of scattering properties of lithosphere of kamchatka based on monte-carlo simulation of record envelope of a near earthquake. *Physics of the earth and Planetary Interiors, 64*(1), 52–67.

Aki, K. (1969). Analysis of the seismic coda of local earthquakes as scattered waves. *Journal of geophysical research*, *74*(2), 615–631.

Aki, K., & Chouet, B. (1975). Origin of coda waves: source, attenuation, and scattering effects. *Journal of geophysical research*, *80*(23), 3322–3342.

Aslan, G., Lasserre, C., Cakir, Z., Ergintav, S., Özarpaci, S., Dogan, U., ... Renard, F. (2019). Shallow creep along the 1999 izmit earthquake rupture (turkey) from gps and high temporal resolution interferometric synthetic aperture radar data (2011–2017). *Journal of Geophysical Research: Solid Earth*, *124*(2), 2218–2236.

Ben-Zion, Y., & Aki, K. (1990). Seismic radiation from an sh line source in a laterally heterogeneous planar fault zone. *Bulletin of the Seismological Society of America*, *80*(4), 971–994.

Ben-Zion, Y., & Sammis, C. G. (2003). Characterization of fault zones. *Pure and Applied Geophysics*, *160*(3-4), 677–715.

Calvet, M., & Margerin, L. (2013). Lapse-time dependence of coda q: Anisotropic multiple-scattering models and application to the pyrenees. *Bulletin of the Seismological Society of America*, *103*(3), 1993–2010.

Campillo, M., & Paul, A. (2003). Long-range correlations in the diffuse seismic coda. *Science*, *299*(5606), 547–549.

Carcolé, E., & Sato, H. (2010). Spatial distribution of scattering loss and intrinsic absorption of short-period s waves in the lithosphere of japan on the basis of the multiple lapse time window analysis of hi-net data. *Geophysical Journal International*, *180*(1), 268–290.

DANA. (2012). *Dense array for north anatolia.* International Federation of Digital Seismograph Networks doi:10.7914/SN/YH2012.

Eulenfeld, T., & Wegler, U. (2017). Crustal intrinsic and scattering attenuation of high-frequency shear waves in the contiguous united states. *Journal of Geophysical Research: Solid Earth*, *122*(6), 4676–4690.

Fehler, M., Hoshiba, M., Sato, H., & Obara, K. (1992). Separation of scattering and intrinsic attenuation for the kanto-tokai region, japan, using measurements of s-wave energy versus hypocentral distance. *Geophysical Journal International*, *108*(3), 787–800.

Fehler, M., & Sato, H. (2003). Coda. *Pure and applied geophysics*, *160*(3-4), 541–

554.

Gusev, A., & Abubakirov, I. (1987). Monte-carlo simulation of record envelope of a near earthquake. *Physics of the Earth and Planetary Interiors*, *49*(1-2), 30–36.

Hirose, T., Nakahara, H., & Nishimura, T. (2019). A passive estimation method of scattering and intrinsic absorption parameters from envelopes of seismic ambient noise cross-correlation functions. *Geophysical Research Letters*, *46*(7), 3634–3642.

Hoshiba, M. (1991). Simulation of multiple-scattered coda wave excitation based on the energy conservation law. *Physics of the Earth and Planetary Interiors*, *67*(1-2), 123–136.

Hoshiba, M. (1993). Separation of scattering attenuation and intrinsic absorption in japan using the multiple lapse time window analysis of full seismogram envelope. *Journal of Geophysical Research: Solid Earth*, *98*(B9), 15809–15824.

Hoshiba, M. (1994). Simulation of coda wave envelope in depth dependent scattering and absorption structure. *Geophysical research letters*, *21*(25), 2853–2856.

Hoshiba, M., Sato, H., & Fehler, M. (1991, 01). Numerical basis of the separation of scattering and intrinsic absorption from full seismogram envelope: A monte-carlo simulation of multiple isotropic scattering. *Papers in Meteorology and Geophysics*, *42*, 65-91. doi: 10.2467/mripapers.42.65

Hu, H., Strybulevych, A., Page, J., Skipetrov, S. E., & van Tiggelen, B. A. (2008). Localization of ultrasound in a three-dimensional elastic network. *Nature Physics*, *4*(12), 945–948.

Jin, A., Mayeda, K., Adams, D., & Aki, K. (1994). Separation of intrinsic and scattering attenuation in southern california using terrascope data. *Journal of Geophysical Research: Solid Earth*, *99*(B9), 17835–17848.

Kahraman, M., Cornwell, D. G., Thompson, D. A., Rost, S., Houseman, G. A., Türkelli, N., ... Gülen, L. (2015). Crustal-scale shear zones and heterogeneous structure beneath the north anatolian fault zone, turkey, revealed by a high-density seismometer array. *Earth and Planetary Science Letters*, *430*, 129–139.

King, G. (1986). Speculations on the geometry of the initiation and termination processes of earthquake rupture and its relation to morphology and geological

684   structure. *Pure and applied geophysics*, *124*(3), 567–585.

685 Lux, I., & Koblinger, L. (1991). *Monte carlo particle transport methods: neutron and*
686   *photon calculations*. CRC Press.

687 Margerin, L., Campillo, M., & Tiggelen, B. (1998). Radiative transfer and diffusion
688   of waves in a layered medium: new insight into coda q. *Geophysical journal in-*
689   *ternational*, *134*(2), 596–612.

690 Mayeda, K., Koyanagi, S., Hoshiba, M., Aki, K., & Zeng, Y. (1992). A comparative
691   study of scattering, intrinsic, and coda q- 1 for hawaii, long valley, and central
692   california between 1.5 and 15.0 hz. *Journal of Geophysical Research: Solid*
693   *Earth*, *97*(B5), 6643–6659.

694 Mayor, J., Margerin, L., & Calvet, M. (2014). Sensitivity of coda waves to spa-
695   tial variations of absorption and scattering: radiative transfer theory and 2-d
696   examples. *Geophysical Journal International*, *197*(2), 1117–1137.

697 Okay, A. I., & Tüysüz, O. (1999). Tethyan sutures of northern turkey. *Geological So-*
698   *ciety, London, Special Publications*, *156*(1), 475–515.

699 Paasschens, J. (1997). Solution of the time-dependent boltzmann equation. *Physical*
700   *Review E*, *56*(1), 1135.

701 Poyraz, S. A., Teoman, M. U., Türkelli, N., Kahraman, M., Cambaz, D., Mutlu, A.,
702   . . . others (2015). New constraints on micro-seismicity and stress state in
703   the western part of the north anatolian fault zone: Observations from a dense
704   seismic array. *Tectonophysics*, *656*, 190–201.

705 Sato, H. (1993a). Energy transportation in one-and two-dimensional scattering me-
706   dia: analytic solutions of the multiple isotropic scattering model. *Geophysical*
707   *Journal International*, *112*(1), 141–146.

708 Sato, H. (1993b). Energy transportation in one-and two-dimensional scattering me-
709   dia: analytic solutions of the multiple isotropic scattering model. *Geophysical*
710   *Journal International*, *112*(1), 141–146.

711 Sato, H. (2019). Isotropic scattering coefficient of the solid earth. *Geophysical Jour-*
712   *nal International*, *218*(3), 2079–2088.

713 Sato, H., Fehler, M. C., & Maeda, T. (2012). *Seismic wave propagation and scatter-*
714   *ing in the heterogeneous earth* (Vol. 496). Springer.

715 Sato, H., Nakahara, H., & Ohtake, M. (1997). Synthesis of scattered energy den-
716   sity for nonspherical radiation from a point shear-dislocation source based on

the radiative transfer theory. *Physics of the earth and planetary interiors*, *104* (1-3), 1–13.

Şengör, A., Tüysüz, O., Imren, C., Sakınç, M., Eyidoğan, H., Görür, N., ... Rangin, C. (2005). The north anatolian fault: A new look. *Annu. Rev. Earth Planet. Sci.*, *33*, 37–112.

Shang, T., & Gao, L. (1988). Transportation theory of multiple scattering and its application to seismic coda waves of impulse source. *Science in China Series B-Chemistry, Biological, Agricultural, Medical & Earth Sciences*, *31* (12), 1503–1514.

Shapiro, N. M., & Campillo, M. (2004). Emergence of broadband rayleigh waves from correlations of the ambient seismic noise. *Geophysical Research Letters*, *31* (7).

Share, P.-E., Allam, A. A., Ben-Zion, Y., Lin, F.-C., & Vernon, F. L. (2019). Structural properties of the san jacinto fault zone at blackburn saddle from seismic data of a dense linear array. *Pure and Applied Geophysics*, *176* (3), 1169–1191.

Shearer, P. M., & Earle, P. S. (2004). The global short-period wavefield modelled with a monte carlo seismic phonon method. *Geophysical Journal International*, *158* (3), 1103–1117.

Singh, S., & Herrmann, R. B. (1983). Regionalization of crustal coda q in the continental united states. *Journal of Geophysical Research: Solid Earth*, *88* (B1), 527–538.

Soergel, D., Pedersen, H., Stehly, L., Margerin, L., Paul, A., & Group, A. W. (2020). Coda-q in the 2.5–20 s period band from seismic noise: application to the greater alpine area. *Geophysical Journal International*, *220* (1), 202–217.

Stehly, L., Campillo, M., Froment, B., & Weaver, R. L. (2008). Reconstructing green's function by correlation of the coda of the correlation (c3) of ambient seismic noise. *Journal of Geophysical Research: Solid Earth*, *113* (B11).

Taylor, G., Rost, S., & Houseman, G. (2016). Crustal imaging across the north anatolian fault zone from the autocorrelation of ambient seismic noise. *Geophysical Research Letters*, *43* (6), 2502–2509.

Taylor, G., Rost, S., Houseman, G. A., Hillers, G., et al. (2019). Near-surface structure of the north anatolian fault zone from rayleigh and love wave tomography using ambient seismic noise. *Solid Earth*.

750 Wegler, U., & Sens-Schönfelder, C. (2007). Fault zone monitoring with passive image
751   interferometry. *Geophysical Journal International*, *168*(3), 1029–1033.

752 Wu, R.-S.   (1985).   Multiple scattering and energy transfer of seismic waves—
753   separation of scattering effect from intrinsic attenuation—i. theoretical mod-
754   elling. *Geophysical Journal International*, *82*(1), 57–80.

755 Wu, R.-S., & Aki, K.   (1988).   Introduction: Seismic wave scattering in three-
756   dimensionally heterogeneous earth.   In *Scattering and attenuations of seismic*
757   *waves, part i* (pp. 1–6). Springer.

758 Yılmaz, Y., Genç, Ş., Yiğitbaş, E., Bozcu, M., & Yılmaz, K.   (1995).   Geological
759   evolution of the late mesozoic continental margin of northwestern anatolia.
760   *Tectonophysics*, *243*(1-2), 155–171.